

1 Local host tree density increases forest insect disturbance severity,
2 but host size effect depends on climatic water deficit

3 Michael J. Koontz^{1,2,*}, Andrew M. Latimer^{1,2}, Leif A. Mortenson³, Christopher J. Fettig³, Malcolm P.
4 North^{1,2,4}

5 ¹Graduate Group in Ecology, University of California, Davis, CA, USA

6 ²Department of Plant Sciences, University of California, Davis, CA, USA

7 ³USDA Forest Service, Pacific Southwest Research Station, Placerville, CA, USA

8 ⁴USDA Forest Service, Pacific Southwest Research Station, Davis, CA, USA

9 *Correspondence: `michael.koontz@colorado.edu` date_generated: !r format(Sys.Date(), "%B %d,
10 %Y")

11 Date report generated:

12 Abstract

13 Bark beetles are a primary mortality agent of trees in western U.S. forests, and the recent Californian hot
14 drought of 2012 to 2015 created favorable conditions for bark beetle-induced tree mortality throughout the
15 yellow pine/mixed-conifer forest system in the Sierra Nevada mountain range. The western pine beetle,
16 *Dendroctonus brevicomis*, is the forest insect that is largely responsible for the especially common deaths of its
17 main host in California, the ponderosa pine tree (*Pinus ponderosa*). While previous work has demonstrated a
18 link between climate conditions related to tree water stress and forest density on the severity of the western
19 pine beetle disturbance, it remains challenging to disentangle the relative effects of these variables. Further,
20 forest density can affect western pine beetle behavior in a number of ways, which creates a need for more
21 information on complex forest structure (including local density, tree size, and the heterogeneity of these
22 variables across a forest stand) to uncover the most likely mechanism.

23 We conducted aerial surveys over an established network of 32 permanent vegetation monitoring plots along
24 a 350km and 1000m elevation gradient in the Sierra Nevada mountain range of California using a small,
25 unhumanned aerial system (sUAS aka drone) equipped with a narrow-band multispectral camera. Using
26 Structure from Motion (SfM) processing on over 450,000 images, we reconstructed the complex vegetation
27 structure of over 9 square kilometers of forest that experienced ponderosa pine mortality as a result of
28 western pine beetle activity. Using this dataset, we built a model to predict the probability of ponderosa
29 pine mortality as a function of forest structure variables (including ponderosa pine density and mean size, as

30 well as all tree density and mean size), an environmental gradient of climatic water deficit, and a Gaussian
31 process to capture spatial covariance in the response.

32 Data from small, unhummaned aerial systems (sUAS) can provide important context surrounding ground
33 plots, which enables inference and generates new insights into ecological processes. sUAS are best-suited to
34 enhancing ground data, which implies that we need not abandon lessons learned from sound experimental
35 design (i.e., a network of plots along a gradient is still a powerful way to use sUAS data).

36 Host availability for aggressive bark beetles appears to have played the dominant role in increasing the probability
37 of ponderosa pine mortality in the most hard-hit forest stands during the cumulative mortality event of 2012 to 2018. Host size played a role in its interaction with environmental condition– climatic
38 water deficit– such that numerous and smaller host trees increased the probability of ponderosa mortality at
40 cool/wet sites, while numerous and larger host trees increased the probability of ponderosa mortality at
41 hot/dry sites.

42 Our results corroborate the role of host tree density and regional climate conditions on the severity of forest
43 insect disturbance, but also highlight the importance of complex forest structure (i.e., both host density and
44 average host size) in its interaction with regional climate. Thus, the future forest structure may be affected
45 differently by a large-scale forest insect disturbance for the same host tree/forest insect pairing, and during
46 the same extreme drought, but across a gradient of regional climate conditions.

47 Introduction

48 Framing: environmental drivers of insect severity, forest structure drivers of insect severity,

49 Aggressive bark beetles dealt the final blow to many of the nearly 150 million trees killed in the California
50 drought of 2012 to 2015 and its aftermath (USDAFS 2019). A harbinger of climate change effects to come,
51 high temperatures exacerbating the extreme drought led to tree mortality events of unprecedented size in the
52 driest, densest forests across the state (Millar and Stephenson 2015, Young et al. 2017). A century of fire
53 suppression policy has enabled forests to grow into dense stands, which increases water stress on trees and
54 makes them more vulnerable to bark beetle attack (Fettig 2012, North et al. 2015).

55 Forests in California’s Sierra Nevada region are characterized by regular bark beetle disturbances that interact
56 with forest structure. Bark beetles shape forest structure as they sporadically kill weakened trees under
57 normal conditions, or wide swaths of even healthy trees under outbreak conditions (Raffa et al. 2015). Forest
58 structure also strongly influences bark beetle activity. Low-density forests are less prone to bark beetle
59 attacks (Fettig 2012), but resolving the mechanism underlying this observation requires a more nuanced view

60 of forest structure. For instance, a low-density forest may resist attack because longer dispersal distances are
61 required for successful colonization of new hosts, because widely-spaced trees experience less competition
62 for water resources and thus average tree vigor is greater (Hayes et al. 2009), or because its wider canopy
63 openings disrupt pheromone signaling between beetles (Fettig 2012).

64 Tree density is often a coarse gauge of the size and spatial distribution of trees— the forest structure— with
65 which bark beetles interact (Raffa et al. 2008). Climate change mitigation strategies emphasize reducing tree
66 densities (North et al. 2015, Young et al. 2017), but understanding the optimal scale and pattern of tree
67 distribution that can mitigate bark beetle outbreaks will be vital for predicting how California forests may
68 respond to these interventions. Recent research has shown a strong link between complex forest structure
69 and forest resilience, but measuring this complexity generally requires expensive equipment or labor-intensive
70 field surveys (Larson and Churchill 2012, Kane et al. 2014). These barriers restrict survey frequency and
71 extent, which limits insights into phenomena like bark beetle outbreaks that rapidly emerge over weeks to
72 months but have long-lasting effects on forest conditions. Further, the vast spatial extent and environmental
73 gradient of mortality (Young et al. 2017, USDAFS 2019) challenges our ability to simultaneously consider
74 how environmental conditions may interact with local forest structure to produce patterns of insect activity.
75 Small, unhumanned aerial systems (sUAS) enable fast and relatively cheap remote imaging over dozens of
76 hectares of forest, which can be used to determine both forest structure and tree condition at the individual
77 tree scale (Morris et al. 2017, Shiklomanov et al. 2019).

78 We used ultra-high resolution remote sensing data from a small, unhumanned aerial system over a network of
79 32 sites in the Sierra Nevada spanning 1000m of elevation and 350km of latitude and covering a total of 9
80 square kilometers of forest to ask how fine-scale forest structure affected the probability of tree mortality
81 during the cumulative mortality event of 2012 to 2018. We asked:

- 82 1. How does local host tree density and size affect the severity of western pine beetle disturbance?
 - 83 2. How does total tree density and size affect the severity of western pine beetle disturbance?
 - 84 3. How does environmentally-driven tree moisture stress affect the severity of western pine beetle distur-
85 bance?
 - 86 4. Do the effects of forest structure and environmental condition on western pine beetle disturbance
87 interact?
- 88 Which trees die during drought? Gradient of stress to host selection. Stephenson et al. (2019) argue that
89 there are differences across species during an extreme drought on whether environment or forest structure

90 drives mortality. But even within the same species, there could be *interaction* between the background
91 environmental condition and the forest struture in driving mortality that gives rise to stress-dominated
92 mortality in some locations and host-selection dominated mortality in other locations *for the same species*.

93 Methods

94 Study system

95 The study sites comprise mostly ponderosa pine trees, *Pinus ponderosa*, whose primary bark beetle predator
96 in California is the western pine beetle (WPB), *Dendroctonus brevicomis*. The WPB is an aggressive bark
97 beetle, meaning it must attack and kill live trees in order to successfully reproduce (Raffa et al. 2008).
98 Pioneer WPBs disperse to a new host tree, determine the host's susceptibility to attack, and use pheromone
99 signals to attract other WPBs. The attracted WPBs mass attack the tree by boring into its inner bark,
100 laying eggs, and dying, leaving their offspring to develop inside the doomed tree before themselves dispersing
101 (Raffa et al. 2008). Small WPB populations prefer weakened trees but large populations can overwhelm
102 the defense mechanisms of even healthy trees. Successful attacks on large, healthy trees are boons to bark
103 beetle fecundity and trigger outbreaks in which populations explode and massive tree mortality occurs. In
104 California, the WPB can have 3 generations in a single year giving it a greater potential to spread rapidly
105 through forests than its more infamous congener, the mountain pine beetle, *Dendroctonus ponderosa* (MPB).

106 We built our study on 180 vegetation/forest insect monitoring plots at 36 sites established between 2016 and
107 2017 (Fettig et al. 2019). These established plots were located in beetle-attacked, mixed-conifer forests across
108 the Eldorado, Stanislaus, Sierra and Sequoia National Forests and were stratified by elevation (914-1219
109 meters [3000-4000 feet], 1219-1524 meters [4000-5000 feet], 1524-1828 meters [5000-6000 feet] above sea level).
110 In the Sequoia National Forest, the National Forest that is furthest south, plots were stratified with the lowest
111 elevation band between 1219 and 1524 (4000-5000 feet) and extended to an upper elevation band of 1828-2133
112 (6000-7000 feet) to capture a more similar forest community composition as at the more northern National
113 Forests. The sites have variable forest structure and disturbance history and plot locations were selected
114 specifically in areas with >40% ponderosa pine basal area and >10% ponderosa pine mortality. The 0.04ha
115 circular plots are clustered along transects in groups of 5, with between 80 and 200m between each plot. All
116 trees within the plot were assessed as dead or alive. The stem location of all trees was mapped relative to the
117 center of each plot using azimuth/distance measurements. Tree identity to species and diameter at breast
118 height (dbh) were recorded if dbh was greater than 6.35cm. During the spring and early summer of 2018, all
119 field plots were revisited to assess whether dead trees had fallen (Fettig et al. 2019).

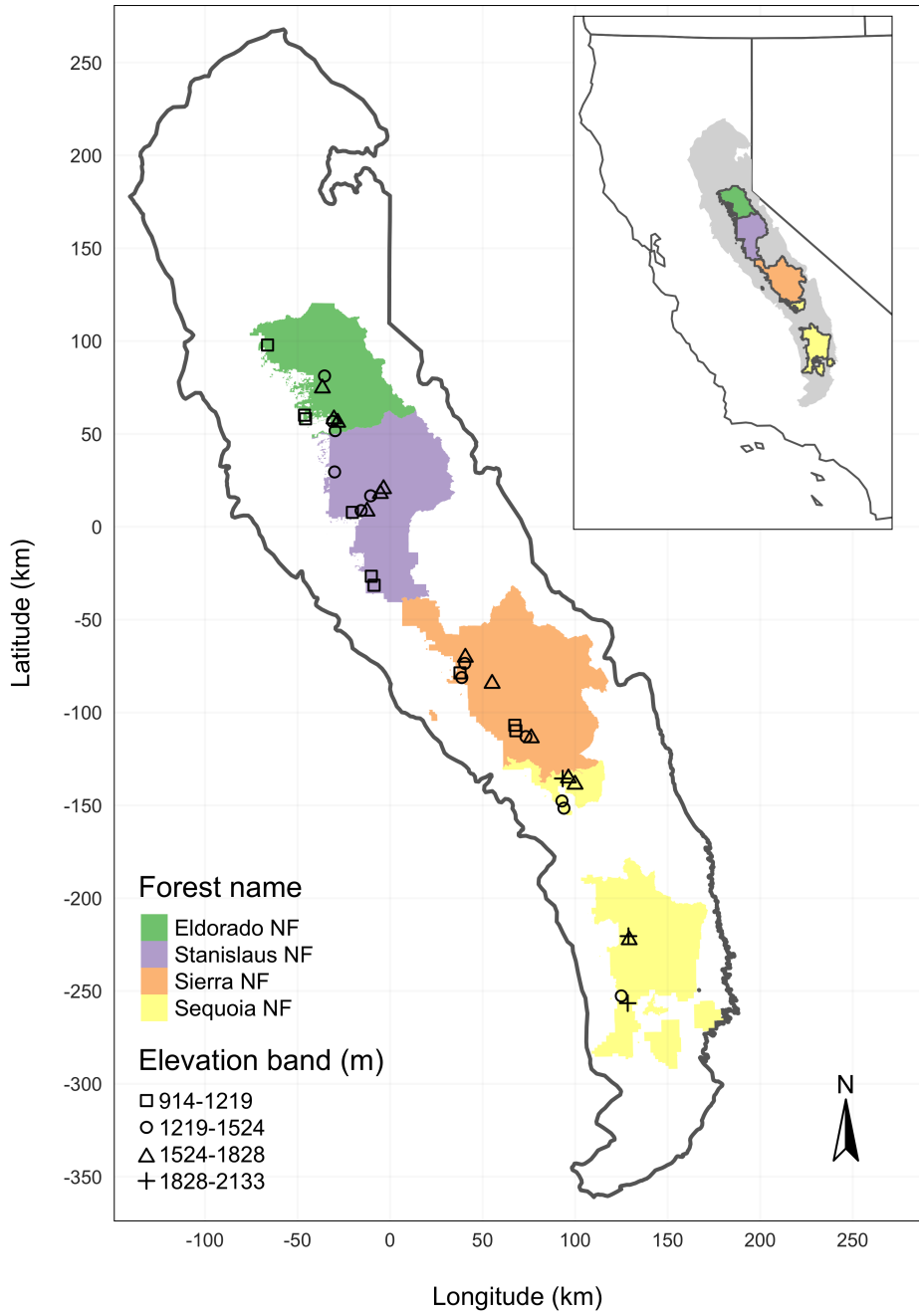


Figure 1: The network of field plots spanned a 350 km latitudinal gradient from the Eldorado National Forest in the north to the Sequoia National Forest in the south. Plots were stratified by three elevation bands in each forest, with the plots in the Sequoia National Forest (the southern-most National Forest) occupying elevation bands 305m above the three bands in the other National Forests in order to capture a similar community composition.

120 **Instrumentation**

121 Imagery was captured using a DJI Zenmuse X3 RGB camera (DJI 2015a) and a Micasense RedEdge3 5-band
122 multispectral camera (Micasense 2015). We mounted both of these instruments simultaneously on a DJI
123 Matrice 100 aircraft (DJI 2015b) using the DJI 3-axis stabilized gimbal for the Zenmuse X3 camera and a
124 Micasense angled fixed mount for the RedEdge3 camera. The gimbal and the angled fixed mount ensured
125 both instruments were nadir-facing during image capture. Just prior or after image capture at each site, we
126 calibrated the RedEdge3 camera by taking an image of a calibration panel on the ground in full sun with
127 known reflectance values for each of the 5 narrow bands.

Table 1: Reflectance sensitivity of the Micasense Rededge3 camera. The calibration panel value represents the reflectance of the calibration panel for the given wavelength.

Band number	Band name	Center wavelength	Band width	Wavelength range	Panel reflectance
1	blue (b)	475	20	465-485	0.64
2	green (g)	560	20	550-570	0.64
3	red (r)	668	10	663-673	0.64
4	near infrared (nir)	840	40	820-860	0.60
5	red edge (re)	717	10	712-722	0.63

128 **Flight protocol**

129 Image capture was conducted as close to solar noon as possible to minimize shadow effects (always within 4
130 hours; usually within 2 hours). Prior to the aerial survey, two strips of bright orange drop cloth (~100cm x
131 15cm) were positioned as an “X” over the permanent monuments marking the center of the 5 field plots from
132 Fettig et al. (2019).

133 For each of the 36 sites (containing 5 plots each), we captured imagery over the surrounding ~40 hectares of
134 forested area using north-south aerial transects. For three sites, we surveyed less surrounding area in order to
135 maintain visual and radio communication with the aircraft during flight which can be obstructed by steep
136 terrain or non-centrally available takeoff locations. (Table 3; as a supplement, I think; Columns: Site, forest,
137 elevation, rep, CWD, surveyed area, survey date).

138 We preprogrammed transect paths using Map Pilot for DJI on iOS (hereafter Map Pilot) (Easy 2018). All
139 transects tracked the terrain and their altitude remained approximately constant at 120 meters above ground

140 level in order to maintain consistent ground sampling distance in the imagery. Ground level was based on a
141 1-arc-second digital elevation model (Farr et al. 2007) and we implemented terrain following using Map Pilot.
142 For this analysis, we dropped 4 sites whose imagery was of insufficient quality to process.

143 Structure from motion (SfM) processing requires highly overlapping images, especially in densely vegetated
144 areas. We planned transects with 90% forward overlap and 90% side overlap at 100 meters below the lens.
145 Thus, with flights being at 120 meters above ground level, we achieved slightly higher than 90/90 overlap for
146 objects 20 meters tall or shorter (91.6/91.6 overlap at the ground). Overlap values were based on focal length
147 (3.6mm), sensor width (6.2mm), and image dimension (4000x3000 pixels) parameters of the Zenmuse X3
148 camera. Images were captured at a constant rate of 1 image every 2 seconds for both cameras. A forward
149 overlap of 90% at 100 meters translates to a flight speed of approximately 6.45 m/s and a side overlap of 90%
150 at 100 meters translates to transects approximately 17.2 meters apart. The Rededge camera has a different
151 focal length (5.4mm), sensor width (4.8mm), and image dimension (1280x960 pixels), which translates to
152 image overlap of 80.7/80.7 at 100m below the lens and 83.9/83.9 at ground level. Approximately 1900 photos
153 were captured over each 40 hectare survey area for each camera.

154 **Structure from motion/Photogrammetric processing**

155 We used structure from motion (SfM), aka photogrammetry, to generate orthorectified reflectance maps,
156 digital surface models, and dense point clouds for each field site. We used Pix4Dmapper Cloud to process
157 imagery using parameters ideal for images of a densely vegetated area taken by a multispectral camera.
158 For three sites, we processed the RGB and the multispectral imagery in the same project to enhance the
159 resolution of the dense point cloud. All SfM projects resulted in a single processing “block,” indicating that
160 all images in the project were optimized and processed together.

161 **Creating canopy height models**

162 We classified each survey area’s dense point cloud into “ground” and “non-ground” points using a cloth
163 simulation filter algorithm (Zhang et al. 2016) implemented in the **lidR** (Roussel et al. 2019) package. We
164 rasterized the ground points using the **raster** package (Hijmans et al. 2019) to create a digital terrain model
165 representing the ground underneath the vegetation at 1 meter resolution. We created a canopy height model
166 by subtracting the digital terrain model from the digital surface model created in Pix4Dmapper.

167 **Tree detection**

168 We tested a total of 7 automatic tree detection algorithms and a total of 177 parameter sets on the canopy
169 height model or the dense point cloud to locate trees within each site (Table 2). We used 3 parameter sets of
170 a variable window filter implemented in **ForestTools** (Plowright 2018) including the default variable window
171 filter function in **ForestTools** as well as the “pines” and “combined” functions from Popescu and Wynne
172 (2004). We used 6 parameter sets of a local maximum filter implemented in **lidR**. We used 131 parameter
173 sets of the algorithm from Li et al. (2012), which operates on the original point cloud. These parameter
174 sets included those from Shin et al. (2018) and Jakubowski et al. (2013). We used 3 parameter sets of the
175 **watershed** algorithm implemented in **lidR**, which is a wrapper for a function in the **EBImage** package (Pau
176 et al. 2010). We used 3 parameter sets of **ptrees** (Vega et al. 2014) implemented in **lidR** (Roussel et al.
177 2019) and **lidRplugins** (Roussel 2019) and which operates on the raw point cloud, without first normalizing
178 it to height above ground level (i.e.. subtracting the ground elevation from the dense point cloud). We used
179 the default parameter set of the **multichm** (Eysn et al. 2015) algorithm implmented in **lidR** (Roussel et
180 al. 2019) and **lidRplugins** (Roussel 2019). We used 30 parameter sets of the experimental algorithm **lmfx**
181 (Roussel 2019).

Table 2: Algorithm name, number of parameter sets tested for each
algorithm, and references.

Algorithm	Parameter sets tested	Reference(s)
li2012	131	Li et al. (2012); Jakubowski et al. (2013); Shin et al. (2018)
lmfx	30	Roussel (2019)
localMaxima	6	Roussel et al. (2019)
multichm	1	Eysn et al. (2015)
ptrees	3	Vega et al. (2014)
vwf	3	Plowright (2018)
watershed	3	Pau et al. (2010)

182 **Map ground data**

183 Each orthorectified reflectance map was inspected to locate the 5 orange “X”s marking the center of the
184 field plots. We were able to locate 110 out of 180 field plots and were then able to use these plots for
185 validation of automated tree detection algorithms. We used the **sf** package (Pebesma et al. 2019) to convert

186 distance-from-center and azimuth measurements of each tree in the ground plots to an x-y position on the
187 SfM-derived reflectance map using the x-y position of the orange X visible in the reflectance map as the
188 center.

189 **Correspondence of automatic tree detection with ground data**

190 We calculated 7 forest structure metrics for each field plot using the ground data collected by Fettig et al.
191 (2019): total number of trees, number of trees greater than 15 meters, mean height of trees, 25th percentile
192 tree height, 75th percentile tree height, mean distance to nearest tree neighbor, mean distance to 2nd nearest
193 neighbor.

194 For each tree detection algorithm and parameter set described above, we calculated the same set of 7 structure
195 metrics within the footprint of the validation field plots. We calculated the Pearson's correlation and root
196 mean square error (RMSE) between the ground data and the aerial data for each of the 7 structure metrics
197 for each of the 177 automatic tree detection algorithms/parameter sets.

198 For each algorithm and parameter set, we calculated its performance relative to other algorithms as whether
199 its Pearson's correlation was within 5% of the highest Pearson's correlation as well as whether its RMSE was
200 within 5% of the lowest RMSE. For each algorithm/parameter set, we summed the number of forest structure
201 metrics for which it reached these 5% thresholds. For automatically detecting trees across the whole study,
202 we selected the algorithm/parameter set that performed well across the most number of forest metrics.

203 **Segmentation of crowns**

204 We delineated individual tree crowns with a marker controlled watershed segmentation algorithm (Meyer and
205 Beucher 1990) using the detected treetops as markers implemented in the `ForestTools` package (Plowright
206 2018). If the automatic segmentation algorithm failed to generate a crown segment for a detected tree (e.g.,
207 often snags with a very small crown footprint), a circular crown was generated with a radius of 0.5 meters. If
208 the segmentation generated multiple polygons for a single detected tree, only the polygon containing the
209 detected tree was retained. Image overlap decreases near the edges of the overall flight path, which reduces
210 the quality of the SfM processing in those areas. Thus, we excluded segmented crowns within 35 meters of
211 the edge of the survey area. Given the narrower field of view of the RedEdge multispectral camera versus
212 the X3 RGB camera whose optical parameters were used to define the ~40 hectare survey area around each
213 site, as well as the 35 meter additional buffering, the survey area at each site was approximately 30 hectares
214 (Table 3).

215 We used the `velox` package (Hunziker 2017) to extract all the pixel values from the orthorectified reflectance

216 map for each of the 5 narrow bands within each segmented crown polygon. Per pixel, we additionally
217 calculated the normalized difference vegetation index (NDVI; Rouse et al. (1973)), the normalized difference
218 red edge (NDRE; Gitelson and Merzlyak (1994)), the red-green index (RGI; Coops et al. (2006)), the red
219 edge chlorophyll index (CI[red edge]; Clevers and Gitelson (2013)), and the green chlorophyll index (CI[green];
220 Clevers and Gitelson (2013)). For each crown polygon, we calculated the mean value for each raw and derived
221 reflectance band (5 raw; 5 derived).

222 **Classification of trees**

223 We overlaid the segmented crowns on the reflectance maps from 20 sites spanning the latitudinal and
224 elevational gradient in the study. Using QGIS, we hand classified 564 trees as live/dead and as one of 5
225 dominant species in the study area (*Pinus ponderosa*, *Pinus lambertiana*, *Abies concolor*, *Calocedrus decurrens*,
226 or *Quercus kelloggii*) using the mapped ground data as a guide.

227 We used all 10 mean values of the reflectance bands for each tree crown polygon to predict whether the hand
228 classified trees were alive or dead using a boosted logistic regression model implemented in the **caret** package
229 (accuracy of live/dead classification on a withheld test dataset: 97.3%) (Kuhn 2008). For just the living trees,
230 we similarly used all 10 reflectance values to predict the tree species using regularized discriminant analysis
231 implemented in the **caret** package (accuracy of species classification on a withheld testing dataset: 66.7%;
232 accuracy of WPB host/non-WPB-host (i.e., ponderosa pine versus other tree species) on a withheld testing
233 dataset: 74.4%).

234 Finally, we used these models to classify all tree crowns in the data set as alive or dead as well as the species
235 of living trees.

236 **Allometric scaling of height to basal area**

237 We converted the height of each tree determined using the canopy height model to its basal area. Using
238 the tree height and diameter at breast height (DBH; breast height = 1.37m) ground data from Fettig et al.
239 (2019), we fit a simple linear regression to predict DBH from height for each of the 5 dominant species. Using
240 the model-classified tree species of each segmented tree, we used the corresponding linear relationship for
241 that species to estimate the DBH given the tree's height. We then calculated each tree's basal area, assuming
242 no tapering from breast height.

243 **Note on assumptions about dead trees**

244 For the purposes of this study, we assumed that all dead trees were ponderosa pine and were thus host trees
245 for the western pine beetle. This is a reasonably good assumption, given that Fettig et al. (2019) found that
246 73.4% of the dead trees in the coincident ground plots were ponderosa pine. The species contributing to
247 the next highest proportion of dead trees was incense cedar which represented 18.72% of the dead trees in
248 the ground plots. Incense cedar is not a potential host of the western pine beetle, and we expand on the
249 limitations of this study given the assumption of dead trees being ponderosa pine in the Discussion.

250 **Rasterizing individual tree data**

251 Because the tree detection algorithms were validated against ground data at the plot level, we rasterized the
252 classified trees at a spatial resolution similar to that of the ground plots (rasterized to 20m x 20m equalling
253 400 m²; circular ground plots with 11.35m radius equalling 404 m²). In each raster cell, we calculated the:
254 number of live trees, number of dead trees, number of ponderosa pine trees, total number of trees (of all
255 species, including ponderosa pine), quadratic mean diameter (QMD) of ponderosa pine trees, and QMD of all
256 trees of any species (overall QMD). We converted the count of ponderosa pine trees and the total tree count
257 to a density measurement of trees per hectare (tpha) by multiplying the counts in each 20m x 20m cell by 25
258 to create a “host density” and an “overall density” variable per cell.

259 **Environmental data**

260 We used climatic water deficit (CWD) (Stephenson 1998) from the 1980-2010 mean value of the basin
261 characterization model (Flint et al. 2013) as an integrated measure of temperature and moisture conditions
262 for each cell. Higher values of CWD correspond to hotter, drier conditions and lower values correspond
263 to cooler, wetter conditions CWD has been shown to correlate well with broad patterns of tree mortality
264 in the Sierra Nevada (Young et al. 2017). We resampled the climatic water deficit product using bilinear
265 interpolation implemented in the `raster` package to match the 20m x 20m spatial scale of the other variables.
266 We converted the CWD value for each cell into a z-score representing that cell’s deviation from the mean
267 CWD across the climatic range of Sierra Nevada ponderosa pine as determined from 179 herbarium records
268 described in Baldwin et al. (2017). Thus, a CWD z-score of one would indicate that the CWD at that
269 cell is one standard deviation hotter/drier than the mean CWD across all geolocated herbarium records for
270 ponderosa pine in the Sierra Nevada.

271 **Statistical model**

272 We used a generalized linear model with a zero-inflated binomial response and a logit link to predict the
 273 probability of ponderosa pine mortality within each raster cell as a function of the crossed effects of ponderosa
 274 pine quadratic mean diameter and density added to the crossed effect of overall quadratic mean diameter and
 275 density as well as the interaction of each summand with climatic water deficit at each site.

276 To measure and account for spatial autocorrelation of the bark beetle behavioral processes underlying
 277 ponderosa mortality, we first subsampled the data at each site to a random selection of 200, 20m x 20m
 278 cells representing approximately 27.5% of the surveyed area. With these subsampled data, we included a
 279 separate exact Gaussian process term per site of the interaction between the x- and y-position of each cell
 280 using the `gp()` function in the `brms` package (Bürkner 2017). The Gaussian process accounts for spatial
 281 autocorrelation in the model by jointly estimating the spatial covariance of the response variable with the
 282 effects of the other covariates.

$$y_{i,j} \sim \begin{cases} 0, & p \\ Binom(n_i, \pi_i), & 1 - p \end{cases}$$

$$\begin{aligned} logit(\pi_i) = & \beta_0 + \\ & \beta_1 X_{cwd,j} + \\ & \beta_1 X_{cwd,j} (\beta_2 X_{\text{pipoQMD},i} + \beta_3 X_{\text{pipoDensity},i} + \beta_4 X_{\text{pipoQMD},i} X_{\text{pipoDensity},i}) + \\ & \beta_1 X_{cwd,j} (\beta_5 X_{\text{overallQMD},i} + \beta_6 X_{\text{overallDensity},i} + \beta_7 X_{\text{overallQMD},i} X_{\text{overallDensity},i}) + \\ & \mathcal{GP}_j(x_i, y_i) \end{aligned}$$

283 Where y_i is the number of dead trees in cell i , n_i is the sum of the dead trees and live ponderosa pine trees
 284 in cell i , π_i is the probability of ponderosa pine tree mortality in cell i , p is the probability of there being
 285 zero dead trees in a cell arising as a result of an unmodeled process, $X_{cwd,j}$ is the z-score of climatic water
 286 deficit for site j , $X_{\text{pipoQMD},i}$ is the scaled quadratic mean diameter of ponderosa pine in cell i , $X_{\text{pipoDensity},i}$
 287 is the scaled density of ponderosa pine trees in cell i , $X_{\text{overallQMD},i}$ is the scaled quadratic mean diameter
 288 of all trees in cell i , $X_{\text{overallDensity},i}$ is the scaled density of all trees in cell i , x_i and y_i are the x- and y-
 289 coordinates of the centroid of the cell in an EPSG3310 coordinate reference system, and \mathcal{GP}_j represents the
 290 exact Gaussian process describing the spatial covariance between cells at site j .

291 We used 4 chains with 2000 iterations each (1000 warmup, 1000 samples), and confirmed chain convergence
 292 by ensuring all `Rhat` values were less than 1.1 (Brooks and Gelman 1998). We used posterior predictive

293 checks to visually confirm model performance by overlaying the density curves of the predicted number of
294 dead trees per cell over the observed number (Gabry et al. 2019). For the posterior predictive checks, we
295 used 50 random samples from the model fit to generate 50 density curves and ensured curves were centered
296 on the observed distribution, paying special attention to model performance at capturing counts of zero.

297 **Software and data availability**

298 All data are available via the Open Science Framework. Statistical analyses were performed using the `brms`
299 packages. With the exception of the SfM software (Pix4Dmapper Cloud) and the GIS software QGIS, all
300 data carpentry and analyses were performed using R (R Core Team 2018).

301 **Results**

Table 3: Site characteristics for each of the 32 sites. The site name consists of the forest name, elevation band, and rep separated by an underscore. The Eldorado National Forest is ‘eldo’, the Stanislaus National Forest is ‘stan’, the Sierra National Forest is ‘sier’, and the Sequoia National Forest is ‘sequ’. The elevation band represents the lower bounds of the 305 meter (1000 foot) elevation bands in feet. Thus ‘3k’ implies that site was located between 3,000 and 4,000 feet (914-1219 meters). Aerially detected mortality and density of the whole site is presented along with the mortality and density calculated from the ground data (aerial / ground). The density is measured in trees per hectare (tpha).

Site	CWD (mm)	CWD (z-score)	Survey area (ha)	Mortality (aerial/ground)	Density (tpha; aerial/ground)
eldo_3k_1	678.45	0.32	31.02	0.11/0.61	630.01/410.19
eldo_3k_2	706.48	0.50	30.61	0.12/0.36	444.26/647.42
eldo_3k_3	654.51	0.16	30.95	0.22/0.36	492.63/410.19
eldo_4k_1	570.43	-0.38	28.04	0.09/0.39	632.82/588.11
eldo_4k_2	642.20	0.08	28.41	0.15/0.78	338.20/271.82
eldo_5k_1	663.09	0.22	28.44	0.11/0.44	661.80/543.63
eldo_5k_2	627.38	-0.01	30.02	0.12/0.36	584.89/968.65
eldo_5k_3	598.66	-0.20	29.73	0.07/0.32	488.66/622.71

Site	CWD (mm)	CWD (z-score)	Survey area (ha)	Mortality (aerial/ground)	Density (tpha; aerial/ground)
stan_3k_1	638.49	0.06	31.04	0.10/0.52	739.45/1037.84
stan_3k_2	739.23	0.71	18.78	0.40/0.78	433.53/405.25
stan_3k_3	761.64	0.86	30.10	0.22/0.41	558.43/326.18
stan_4k_1	540.16	-0.58	29.62	0.29/0.63	507.61/711.66
stan_4k_2	528.07	-0.66	30.54	0.18/0.56	481.85/256.99
stan_5k_1	523.51	-0.69	30.94	0.19/0.54	388.89/336.06
stan_5k_2	523.95	-0.68	29.94	0.21/0.44	399.33/622.71
sier_3k_1	763.54	0.87	30.42	0.19/0.48	651.46/850.04
sier_3k_2	767.64	0.90	30.05	0.20/0.77	438.84/153.21
sier_3k_3	772.98	0.93	29.77	0.32/0.77	511.26/459.62
sier_4k_1	841.25	1.38	30.43	0.54/0.51	576.15/538.69
sier_4k_2	764.38	0.88	29.30	0.33/0.57	499.43/854.98
sier_4k_3	688.34	0.38	26.39	0.48/0.59	454.23/499.15
sier_5k_1	721.59	0.60	14.59	0.41/0.43	631.30/716.60
sier_5k_2	709.96	0.52	27.53	0.53/0.74	477.29/454.67
sier_5k_3	778.53	0.97	28.93	0.33/0.43	569.44/484.33
sequ_4k_1	766.61	0.89	29.59	0.50/0.56	365.81/607.88
sequ_4k_3	815.60	1.21	29.69	0.35/0.71	433.35/306.41
sequ_5k_1	718.24	0.58	27.12	0.35/0.52	364.01/444.79
sequ_5k_2	587.26	-0.27	29.10	0.45/0.43	478.31/499.15
sequ_5k_3	611.33	-0.12	31.34	0.42/0.48	348.68/494.21
sequ_6k_1	730.52	0.66	27.78	0.30/0.70	433.43/360.77
sequ_6k_2	689.51	0.39	11.83	0.26/0.43	699.04/934.06
sequ_6k_3	602.65	-0.17	26.51	0.36/0.32	535.54/691.89

302 **Tree detection**

303 We found that the experimental `lmfx` algorithm with parameter values of `dist2d = 1` and `ws = 2.5` (Roussel
 304 et al. 2019) performed the best across 7 measures of forest structure as measured by Pearson's correlation
 305 with ground data (Table 3).

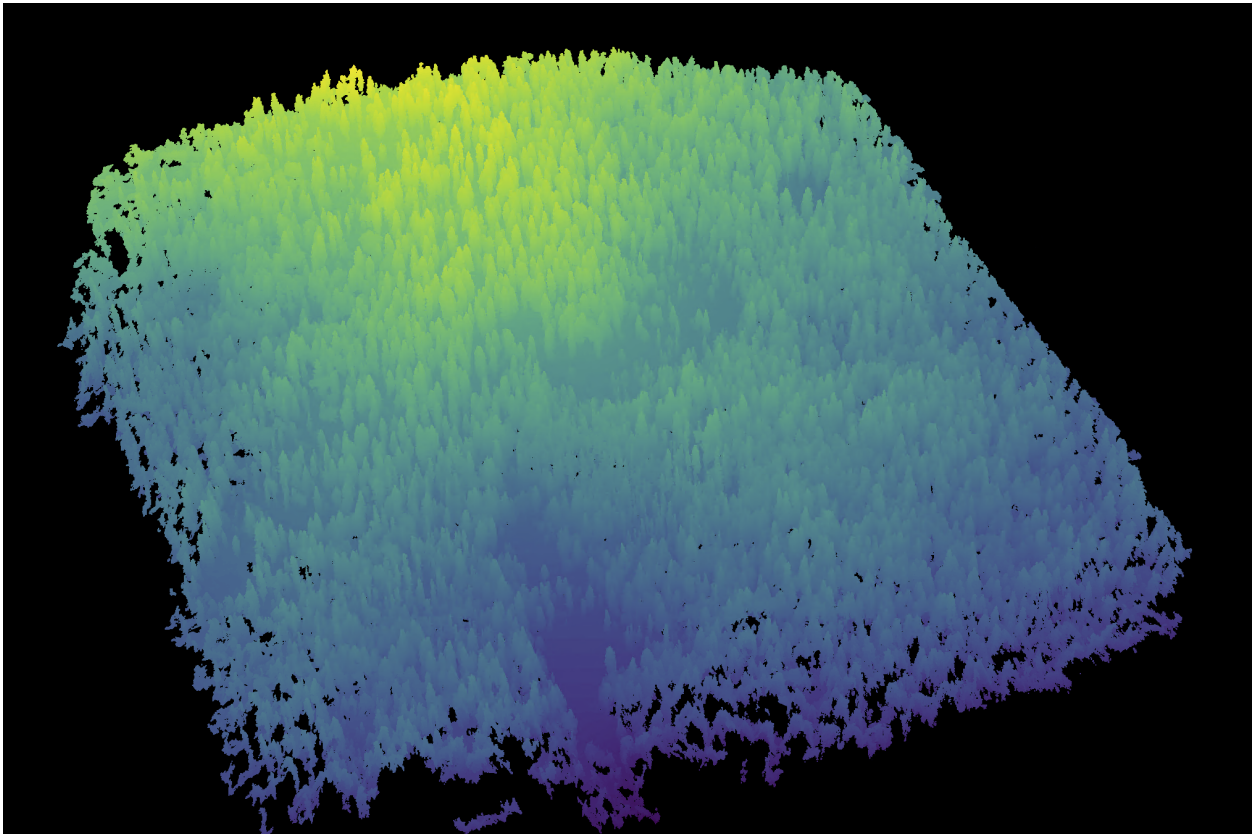


Figure 2: A dense point cloud representing ~40 hectares of forest is generated using Structure from Motion (SfM) processing of ~1900 images. The dense point cloud z- position represents the ground elevation plus the vegetation height.

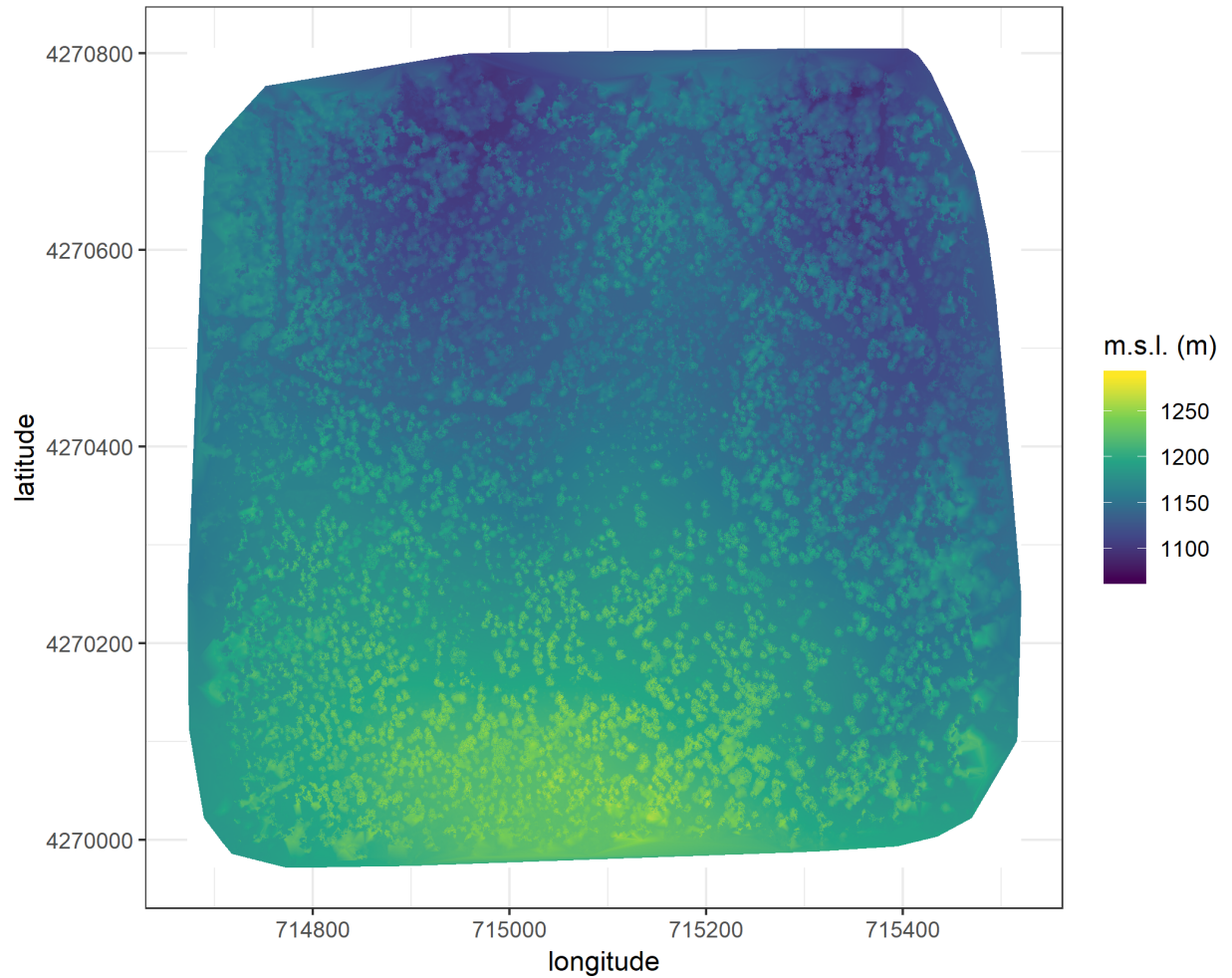


Figure 3: The digital surface model (DSM) is a 2-dimensional representation of the dense point cloud generated using structure from motion (SfM) processing. The DSM represents the ground elevation plus the vegetation height.

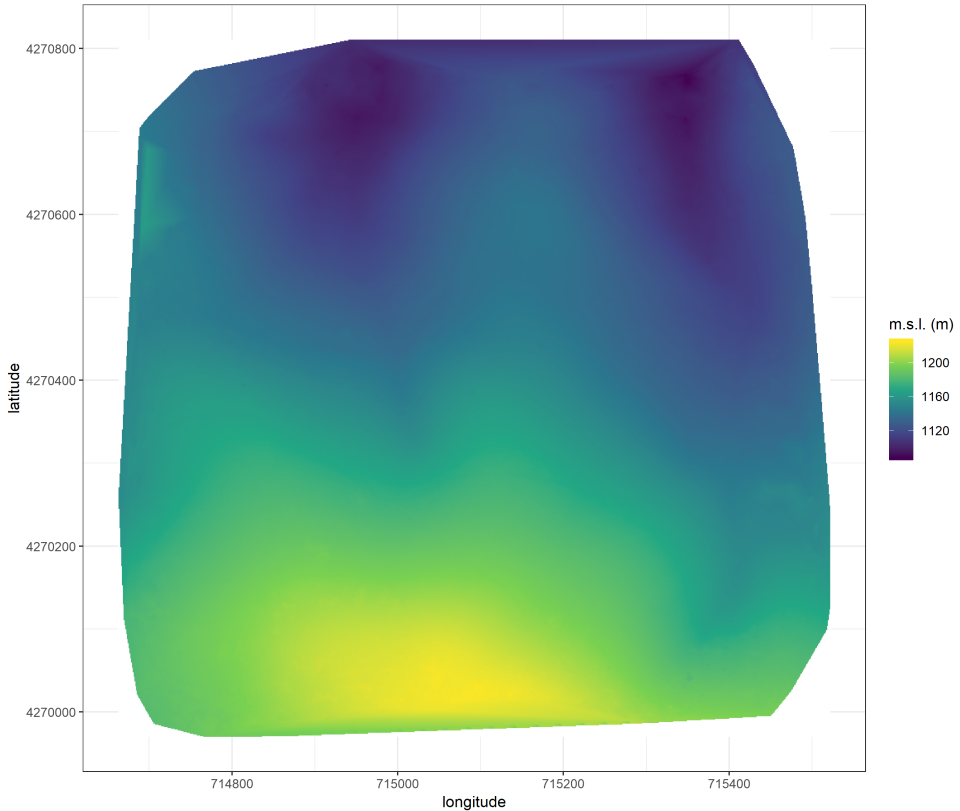


Figure 4: The digital terrain model (DTM) is generated by processing the dense point cloud using the cloth simulation filter algorithm (Zhang et al. 2016), which classifies points as “ground” or “not-ground” and then interpolates the “ground” elevation using Delaunay triangulation for the rest of the dense point cloud footprint. The DTM represents the ground elevation without any vegetation.

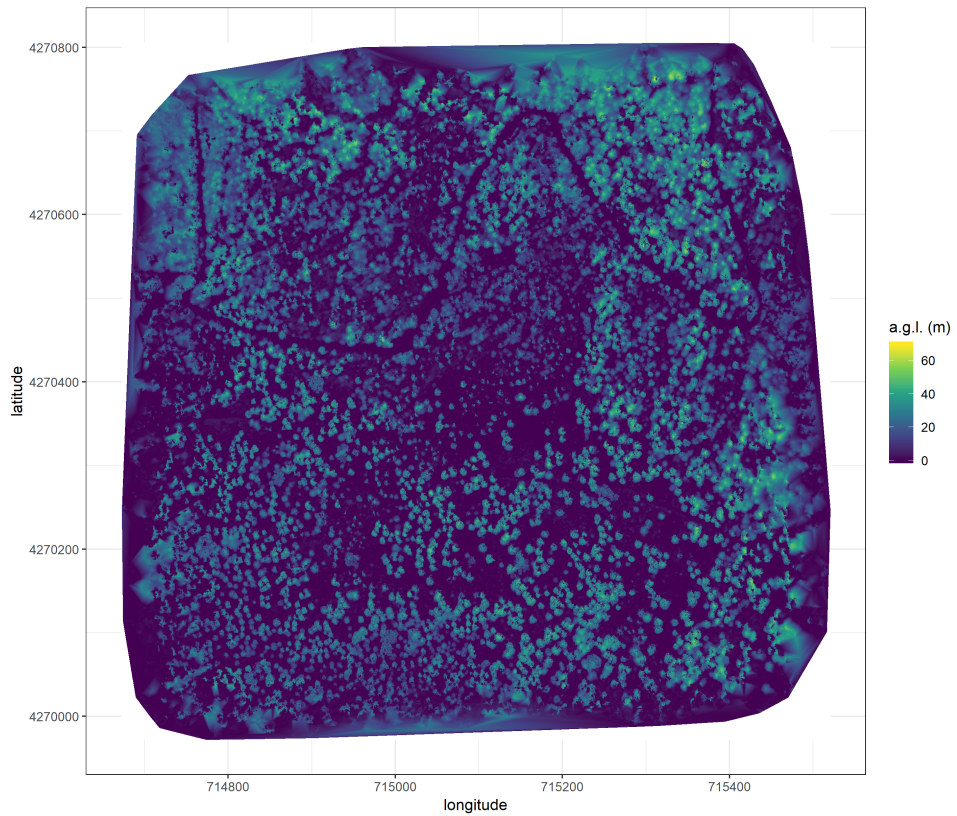


Figure 5: The canopy height model (CHM) is generated by subtracting the digital terrain model from the digital surface model. The CHM represents the height of all of the elevation above ground level.

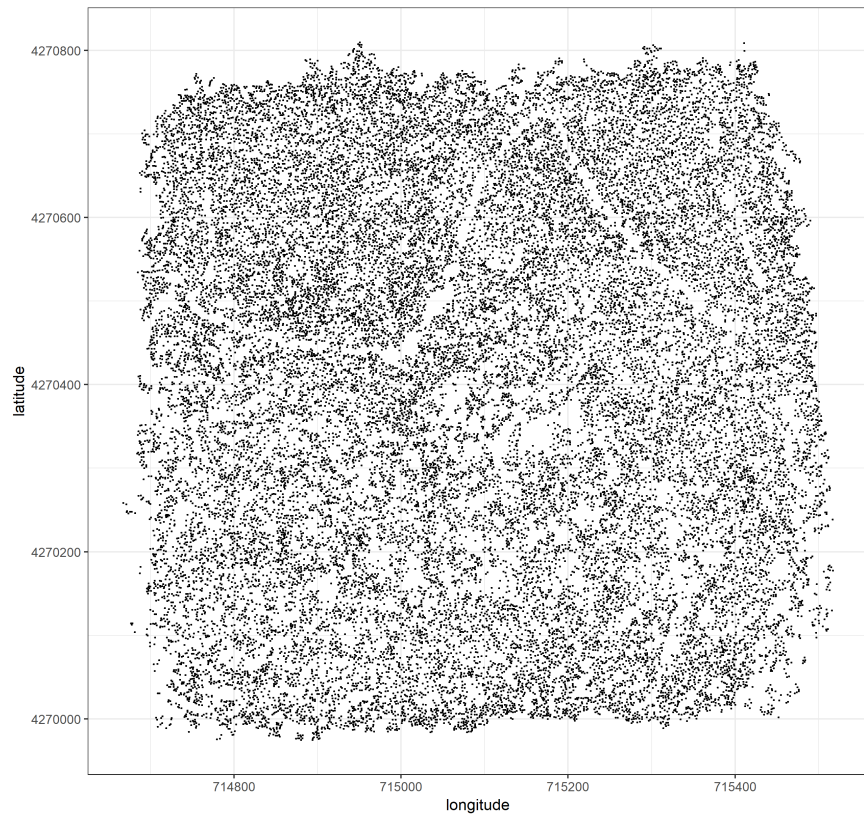


Figure 6: Tree locations are detected using the `lmfx` (Roussel et al. 2019) treetop detection algorithm on the dense point cloud.

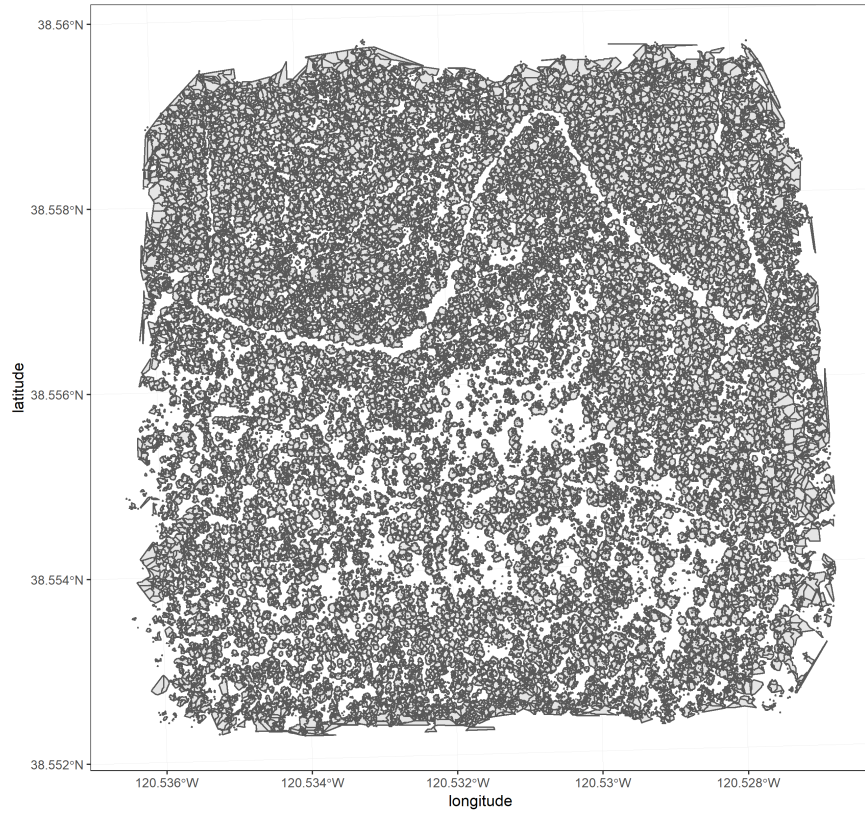


Figure 7: Individual crowns are delineated using a marker controlled watershed segmentation algorithm (Meyer and Beucher 1990, Plowright 2018) on the canopy height model (CHM) using the detected tree locations as a priority map. If the algorithm failed to delineate a crown for a tree that was identified in the tree detection step, a circular crown with a 0.5m buffer centered on point location of the detected tree was added as a crown.

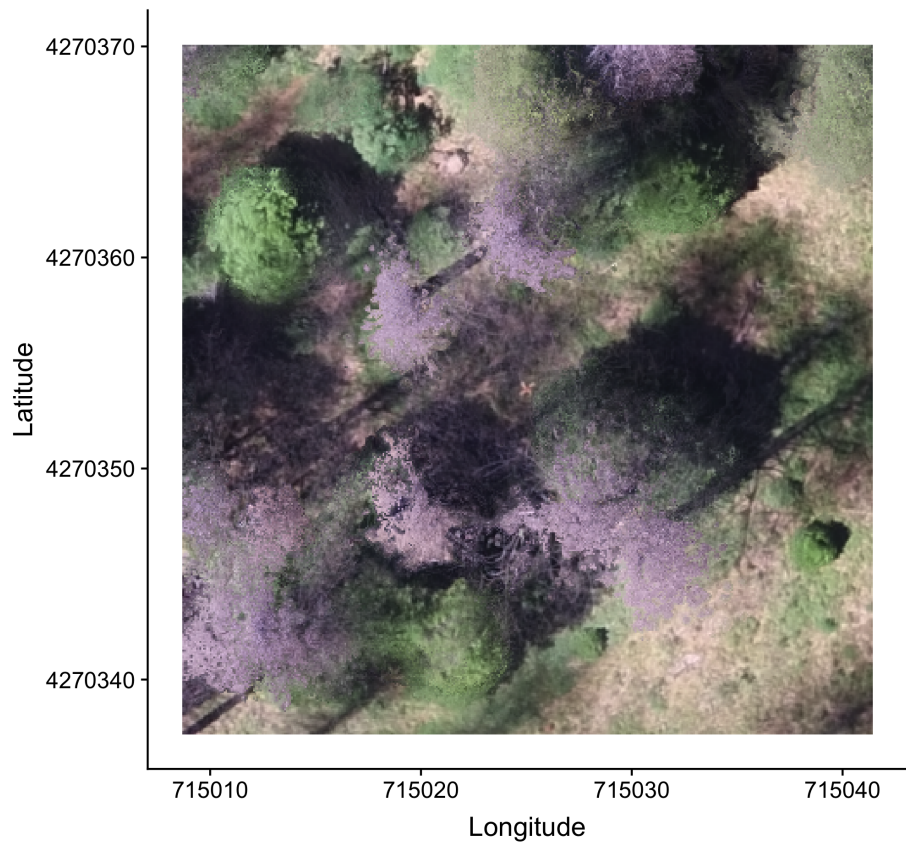


Figure 8: The orthomosaic for each of the 32 sites is generated with the Structure from Motion (SfM) processing, showing a top-down view of the whole survey area such that distances between objects in the scene are preserved and can be measured. Depicted is an example orthomosaic for one of the 32 sites cropped to the extent of a single ground plot (5 ground plots per site) showing the orange X placed at exactly the plot center prior to flight. The original orthomosaic for the whole site represents an area approximately 1000 times as large as the area depicted here.

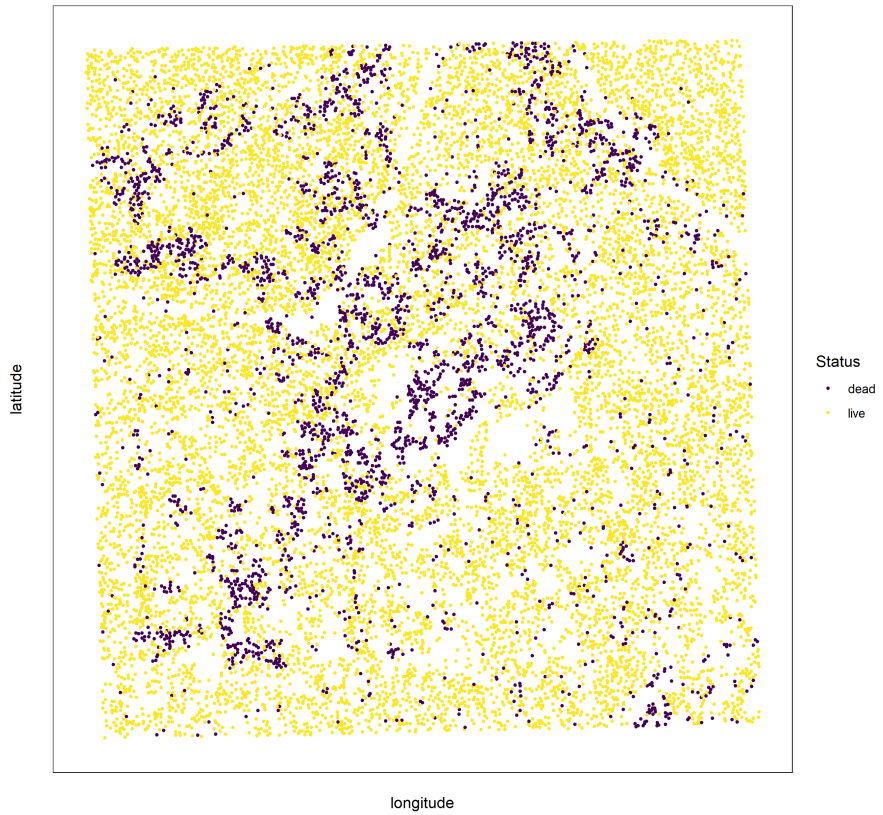


Figure 9: Each tree is classified as live or dead by extracting the pixel values from the 5 narrow bands of the Rededge3 camera (and 5 derived bands— see methods) in the orthomosaic within each segmented tree crown of the detected trees, taking their mean value, and using those means to predict live/dead status with a boosted logistic regression previously trained on a hand-classified set of segmented crowns from across the study area.

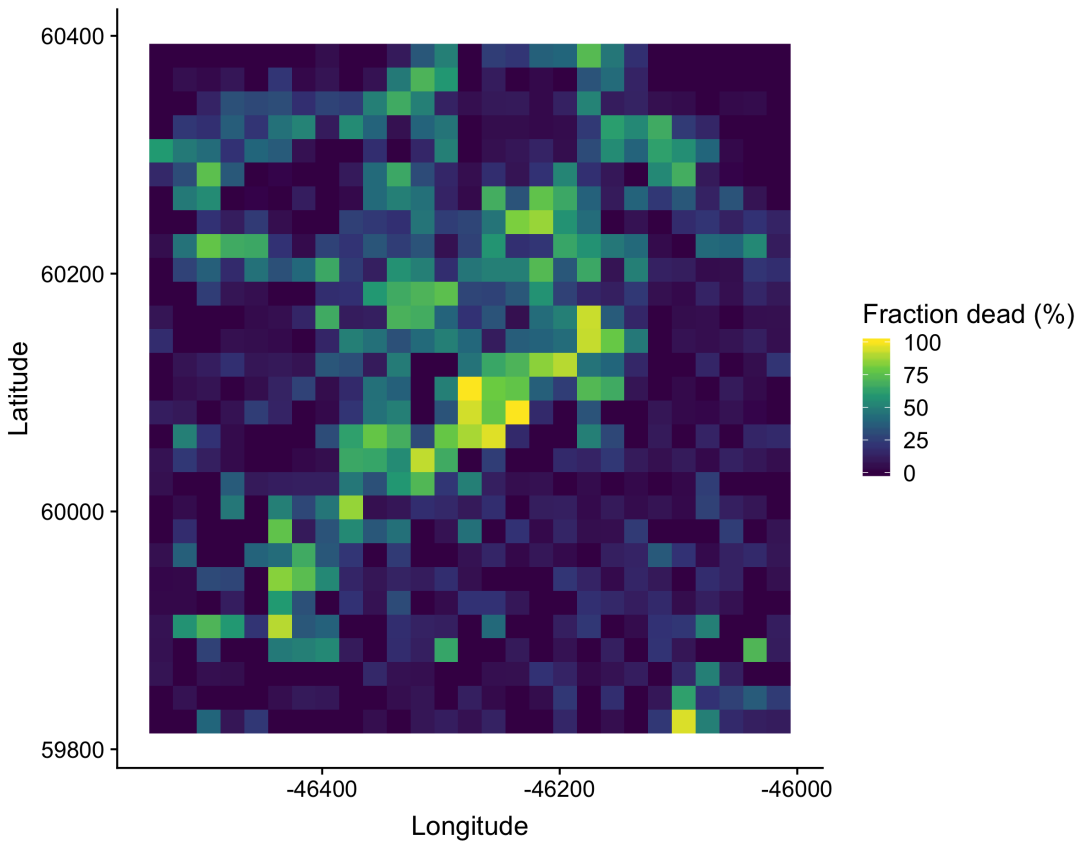


Figure 10: We rasterized the individual tree data by aggregating values to 20m x 20m cells. This example shows the proportion of dead trees per cell for the same example site as in the previous figures.

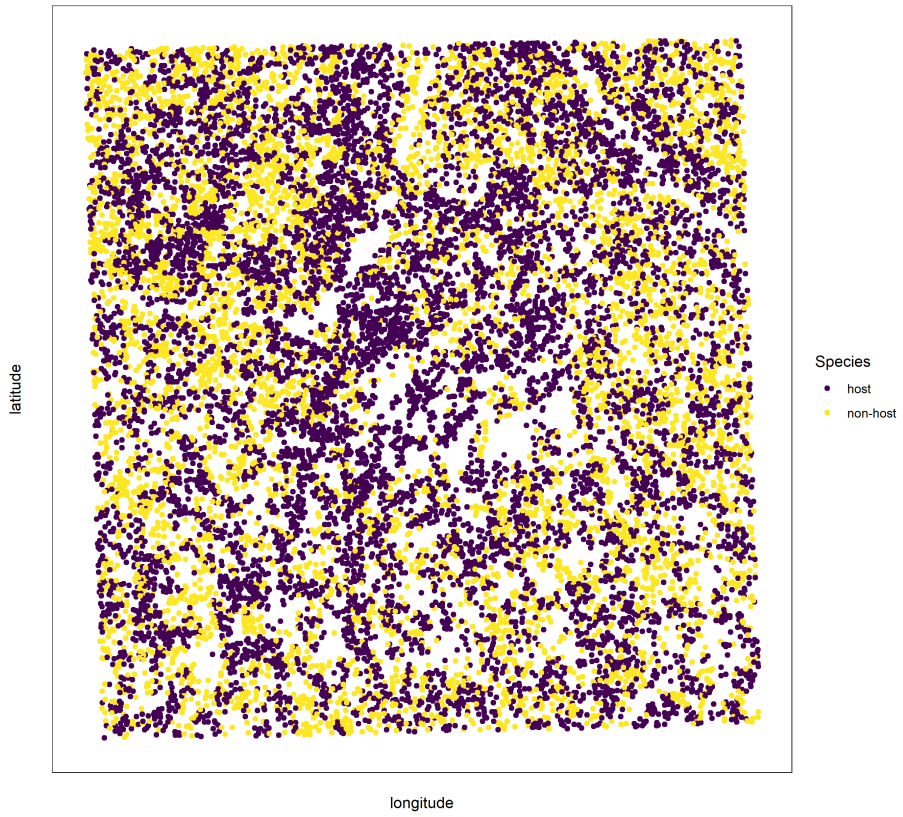


Figure 11: For each live tree, we classified its species using the same means of extracted pixel values across the 5 Rededge3 narrow bands (and 5 derived bands) as predictors in a regularized discriminant analysis previously trained on a hand-classified set of segmented crowns from across the study area. Host/non-host data were also rasterized as in the previous figure prior to analyses (not shown).

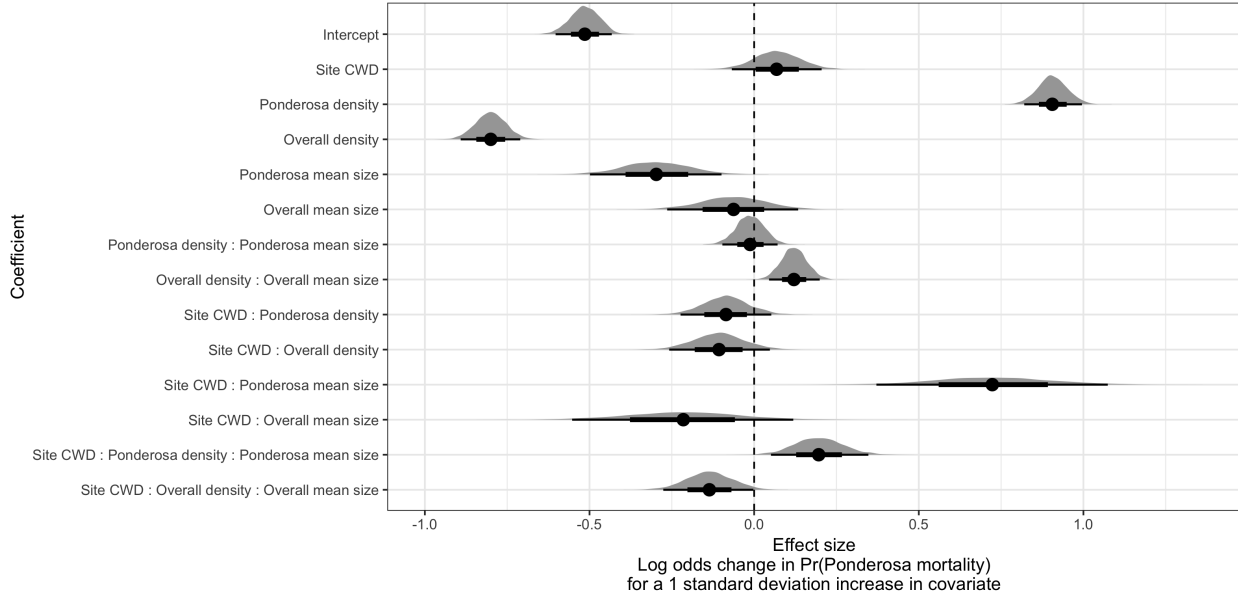


Figure 12: Posterior distributions of effect size from zero-inflated binomial model predicting the probability of ponderosa pine mortality in a 20m x 20m cell given forest structure characteristics of host trees and all trees within the cell, as well as a site-level climatic water deficit. The gray density distribution for each model covariate represents the density of the posterior distribution, the point underneath each density curve represents the median of the estimate, the bold interval surrounding the point estimate represents the 66% credible interval, and the thin interval surrounding the point estimate represents the 95% credible interval.

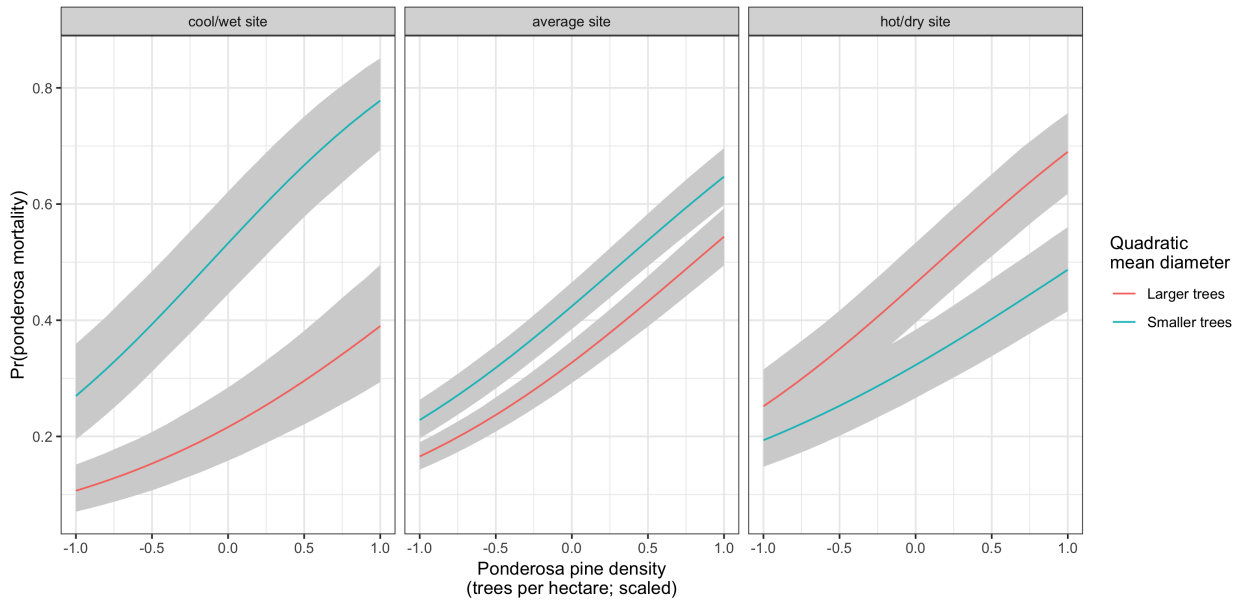


Figure 13: Line version of model results with 95% credible intervals showing primary influence of ponderosa pine structure on the probability of ponderosa pine mortality, and the interaction across climatic water deficit. The “larger trees” line represents the quadratic mean diameter of ponderosa pine 0.7 standard deviations above the mean, and the “smaller trees” line represents the quadratic mean diameter of ponderosa pine 0.7 standard deviations below the mean.

Table 4: Correlation and differences between the best performing tree detection algorithm (lmfx with dist2d = 1 and ws = 2.5) and the ground data. An asterisk next to the correlation or RMSE indicates that this value was within 5% of the value of the best-performing algorithm/parameter set. Ground mean represents the mean value of the forest metric across the 110 ground plots that were visible from the sUAS-derived imagery. The median error is calculated as the median of the differences between the air and ground values for the 110 visible plots. Thus, a positive number indicates an overestimate by the sUAS workflow and a negative number indicates an underestimate.

Forest structure metric	Ground mean	Correlation with ground	RMSE	Median error
total tree count	18.52	0.67*	8.68*	2.00
count of trees > 15m	9.89	0.43	7.38	0.00
dist to 1st nearest neighbor (m)	2.82	0.55*	1.16*	0.26
dist to 2nd nearest neighbor (m)	4.30	0.61*	1.70*	0.12
height (m); 25th percentile	12.42	0.16	8.46	-1.16
height (m); mean	18.49	0.29	7.81*	-2.29
height (m); 75th percentile	24.55	0.35	10.33*	-3.98

306 Effect of local structure and regional climate on western pine beetle severity

307 We detected no main effect of climatic water deficit on the probability of ponderosa pine mortality within
308 each 20m x 20m cell.

309 We found a strong main effect of ponderosa pine local density, accounting for quadratic mean diameter of
310 ponderosa pine, with greater density increasing the probability of ponderosa pine mortality.

311 Conversely, we found a generally negative effect of quadratic mean diameter of ponderosa pine on the
312 probability of ponderosa mortality, suggesting that the western pine beetle attacked smaller trees, on average.

313 There was a strong positive interaction between the climatic water deficit and ponderosa pine quadratic mean
314 diameter, such that larger trees were more likely to increase the probability of ponderosa mortality in hotter,
315 drier sites.

316 We found negative main effects of overall tree density and overall quadratic mean diameter. There was a
317 positive interaction between these variables, such that denser stands with larger trees did lead to greater
318 ponderosa pine mortality.

319 **Spatial effects**

320 We were able to calculate the length scale of the spatial autocorrelation in the probability of ponderosa
321 pine mortality at each site, accounting for forest structure and environmental factors. By fitting a separate
322 approximate Gaussian process for each site on the interacting variables of the x- and y- position, we measured
323 the spatial covariance inherent in the data, accounting for other factors. ## Discussion

324 **Closer spacing between potential host trees facilitates dispersal**

325 If this drives mortality patterns, then we'd expect the local density of ponderosa pine trees, accounting for
326 other variables, to have a strong positive effect.

327 **Host preference for large trees**

328 If this drives mortality patterns, then we'd expect the quadratic mean diameter of ponderosa pine trees,
329 accounting for other variables, to have a strong positive effect.

330 **Denser forests augment pheromone communication**

331 If this drives mortality patterns, then we'd expect the local density of all trees, accounting for other variables,
332 to have a strong positive effect.

333 **Tree crowding leads to greater average water stress per tree**

334 If this drives mortality patterns, then we'd expect the quadratic mean dimater of all trees, accounting for
335 other factors, to have a strong positive effect.

336 **Interaction between host density and host size**

337 A positive coefficient would indicate a combined effect of WPB preference for large trees and nearby host
338 availability.

339 **Interaction between all tree density and all tree size**

340 A positive coefficient would indicate a combined effect of tree crowding and pheromone communication
341 enhancement.

342 Implications of forest structure/regional climate interactions

343 We found that the probability of ponderosa pine mortality generally increased with local host availability
344 (host density), but also interacted with both host size and regional climate such that the role of tree size
345 became increasingly important in more climatically extreme sites. A smaller average tree size led to a lower
346 probability of ponderosa mortality in cool/wet sites and a larger average tree size led to a greater probability
347 of ponderosa mortality in hot/dry sites. These mortality patterns highlight a possible distinction in behavior
348 between the recent western bark beetle activity across the gradient of climatic water deficit. Even in the most
349 highly impacted forest stands (because our study sites were selected conditional on there being high levels of
350 western pine beetle activity), there is still a detectable effect of tree size such that the smaller (presumably
351 weaker) trees are getting killed in cooler/wetter sites, and the larger (presumably more well-defended) trees
352 are getting killed more in the hotter/drier sites. So while mortality is high everywhere, there does appear to
353 be a difference in the beetle choosiness across the climatic water deficit gradient.

354 Similarities and differences with Fettig et al. (2019)

355 Fettig et al. (2019) found positive relationship between number of trees killed and: total number of trees,
356 total basal area, stand density index.

357 Fettig et al. (2019) found negative relationship between the proportion of trees killed and: total number of
358 trees, stand density index.

359 Hayes et al. (2009) and Fettig et al. (2019) found measures of host availability explained less variation in
360 mortality than measures of stand density.

361 Negrón et al. (2009) reported positive association of probability of ponderosa pine mortality and tree density
362 during a drought in Arizona.

363 Effect of competition may be masked because drought was so extreme Fettig et al. (2019); Floyd et al.
364 (2009), which is perhaps why we saw a counter-intuitive signal of increasing total basal area leading to lower
365 probability of ponderosa pine mortality.

366 Broader context around field plots

367 We surveyed 9 square kilometers of forest representing ~450,000 trees along a broad environmental gradient
368 of climatic water deficit. Site selection and small plot size can influence inference. For instance, Fettig et
369 al. (2019) reported statistically undetectable differences in overall mortality in their plot network across 4
370 national forests. By expanding the hectarage surveyed by a factor of 200, we detected dramatic differences in

371 overall mortality.

372 This is about more than sample size (though that helps). This is also about capturing the local disturbance
373 phenomenon.

374 **Implications for future forest structure**

375 We have demonstrated that forest structure (local host density and size) affected the cumulative severity
376 of the western pine beetle in the Sierra Nevada in the 2012 to 2015 drought and its aftermath. Clearly,
377 this forest insect disturbance has reciprically impacted the forest structure, with uncertain consequences for
378 long-term forest dynamics.

379 Small trees are getting killed in cooler/wetter sites, larger trees getting killed in hotter/drier sites. Perhaps
380 the cooler/wetter sites are resisting even this massive disturbance event?

381 **Spatial effect**

382 The western pine beetle is known to exhibit strong aggregation and anti-aggregation behavior arising from
383 its pheromone communication, and thus it is likely that the measured spatial covariance in this study is
384 attributable in part to the magnitude of this effect at each site.

385 Some studies have suggested that “outbreak” conditions are distinguishable by clustered tree mortality, but
386 this is perhaps challenging to tease apart (Raffa et al. 2008). Our modeling framework allows for a joint
387 estimation of the effects of forest structure, environmental condition, and the spatial effect. This framework
388 would be enhanced with confidence in individual tree level data, and a lot of it, along with a strong gradient
389 of environmental conditions and forest structure.

390 We won’t interpret this measure of contagion, because the uncertainties in this particular study are too great
391 (tree detection, species classification, dead trees all assumed to be WPB hosts, didn’t account for topographic
392 effects which could also manifest as part of this spatial covariance process). We do suggest that this could be
393 a meaningful and quantifiable means of assessing bark beetle “stage of outbreak”.

394 **Future spatial directions (will cut this; here for now so I can write it down elsewhere)**

395 Perhaps could also compare relative effect of individual tree spacing (Voronoi polygon area) with the length
396 scale parameter at a certain site to get at a similar question. A big voronoi polygon area effect and a short
397 covariance kernel tells us that it’s a water stress effect– a crowded tree gets attacked regardless of whether
398 nearby trees were attacked. A small voronoi polygon area effect and a long covariance kernel tells us that the

399 mortality is patterned more based on there being spillover from nearby attacked neighbors instead of how
400 crowded any given tree is. I expect we might see different relative magnitudes of voronoi polygon area and
401 covariance kerenel effects depending on CWD.

402 **Important considerations**

403 Cumulative effect of elevated insect activity, as mortality was spread out over 5 years and we surveyed at the
404 end. All the detected dead trees were considered ponderosa pine– we know this is wrong. Only about 3 out
405 of 4 dead trees in Fettig et al. (2019) were ponderosa.

406 **Room for improvement**

- 407 • Better geometry by using higher overlap, more spatially resolved images.
- 408 • Better image classification and scalability by using instrumentation having spectral overlap with more
409 widely deployed instrumentation (e.g., Landsat).
- 410 • Better tree detection using machine learning approaches
- 411 • Our live/dead classifier works pretty well.
- 412 • Our species classifier could improve. Perhaps also using machine learning approaches.

413 (Seidl et al. 2015) (Preisler et al. 2017)

414 **References**

- 415 Baldwin, B. G., A. H. Thornhill, W. A. Freyman, D. D. Ackerly, M. M. Kling, N. Morueta-Holme, and B. D.
416 Mishler. 2017. Species richness and endemism in the native flora of California. American Journal of Botany
417 104:487–501.
- 418 Brooks, S. P., and A. Gelman. 1998. General Methods for Monitoring Convergence of Iterative Simulations.
419 Journal of Computational and Graphical Statistics 7:434.
- 420 Bürkner, P.-C. 2017. **Brms** : An *R* Package for Bayesian Multilevel Models Using *Stan*. Journal of Statistical
421 Software 80.
- 422 Clevers, J., and A. Gitelson. 2013. Remote estimation of crop and grass chlorophyll and nitrogen content using
423 red-edge bands on Sentinel-2 and -3. International Journal of Applied Earth Observation and Geoinformation
424 23:344–351.
- 425 Coops, N. C., M. Johnson, M. A. Wulder, and J. C. White. 2006. Assessment of QuickBird high spatial
426 resolution imagery to detect red attack damage due to mountain pine beetle infestation. Remote Sensing of

- 427 Environment 103:67–80.
- 428 DJI. 2015a. Zenmuse X3 - Creativity Unleashed. <https://www.dji.com/zenmuse-x3/info>.
- 429 DJI. 2015b. DJI - The World Leader in Camera Drones/Quadcopters for Aerial Photography. <https://www.dji.com/matrice100/info>.
- 430
- 431 Easy, D. M. 2018. Map Pilot for DJI. <https://itunes.apple.com/us/app/map-pilot-for-dji/id1014765000?mt=8>.
- 432 Eysn, L., M. Hollaus, E. Lindberg, F. Berger, J.-M. Monnet, M. Dalponte, M. Kobal, M. Pellegrini, E.
- 433 Lingua, D. Mongus, and N. Pfeifer. 2015. A Benchmark of Lidar-Based Single Tree Detection Methods Using
- 434 Heterogeneous Forest Data from the Alpine Space. Forests 6:1721–1747.
- 435 Farr, T. G., P. A. Rosen, E. Caro, R. Crippen, R. Duren, S. Hensley, M. Kobrick, M. Paller, E. Rodriguez, L.
- 436 Roth, D. Seal, S. Shaffer, J. Shimada, J. Umland, M. Werner, M. Oskin, D. Burbank, and D. Alsdorf. 2007.
- 437 The Shuttle Radar Topography Mission. Reviews of Geophysics 45.
- 438 Fettig, C. J. 2012. Chapter 2: Forest health and bark beetles. *in* Managing Sierra Nevada Forests. PSW-
- 439 GTR-237. USDA Forest Service.
- 440 Fettig, C. J., L. A. Mortenson, B. M. Bulaon, and P. B. Foulk. 2019. Tree mortality following drought in the
- 441 central and southern Sierra Nevada, California, U.S. Forest Ecology and Management 432:164–178.
- 442 Flint, L. E., A. L. Flint, J. H. Thorne, and R. Boynton. 2013. Fine-scale hydrologic modeling for regional land-
- 443 scape applications: The California Basin Characterization Model development and performance. Ecological
- 444 Processes 2:25.
- 445 Floyd, M. L., M. Clifford, N. S. Cobb, D. Hanna, R. Delph, P. Ford, and D. Turner. 2009. Relationship of
- 446 stand characteristics to drought-induced mortality in three Southwestern piñonJuniper woodlands. Ecological
- 447 Applications 19:1223–1230.
- 448 Gabry, J., D. Simpson, A. Vehtari, M. Betancourt, and A. Gelman. 2019. Visualization in Bayesian workflow.
- 449 Journal of the Royal Statistical Society: Series A (Statistics in Society) 182:389–402.
- 450 Gitelson, A., and M. N. Merzlyak. 1994. Spectral Reflectance Changes Associated with Autumn Senescence
- 451 of Aesculus hippocastanum L. and Acer platanoides L. Leaves. Spectral Features and Relation to Chlorophyll
- 452 Estimation. Journal of Plant Physiology 143:286–292.
- 453 Hayes, C. J., C. J. Fettig, and L. D. Merrill. 2009. Evaluation of Multiple Funnel Traps and Stand
- 454 Characteristics for Estimating Western Pine Beetle-Caused Tree Mortality. Journal of Economic Entomology

- 455 102:2170–2182.
- 456 Hijmans, R. J., J. van Etten, M. Sumner, J. Cheng, A. Bevan, R. Bivand, L. Busetto, M. Canty, D. Forrest,
457 A. Ghosh, D. Goliche, J. Gray, J. A. Greenberg, P. Hiemstra, I. for M. A. Geosciences, C. Karney, M.
458 Mattiuzzi, S. Mosher, J. Nowosad, E. Pebesma, O. P. Lamigueiro, E. B. Racine, B. Rowlingson, A. Shortridge,
459 B. Venables, and R. Wueest. 2019. *Raster: Geographic Data Analysis and Modeling*.
- 460 Hunziker, P. 2017. *Velox: Fast Raster Manipulation and Extraction*.
- 461 Jakubowski, M. K., W. Li, Q. Guo, and M. Kelly. 2013. Delineating Individual Trees from Lidar Data: A
462 Comparison of Vector- and Raster-based Segmentation Approaches. *Remote Sensing* 5:4163–4186.
- 463 Kane, V. R., M. P. North, J. A. Lutz, D. J. Churchill, S. L. Roberts, D. F. Smith, R. J. McGaughey, J. T.
464 Kane, and M. L. Brooks. 2014. Assessing fire effects on forest spatial structure using a fusion of Landsat and
465 airborne LiDAR data in Yosemite National Park. *Remote Sensing of Environment* 151:89–101.
- 466 Kuhn, M. 2008. Building Predictive Models in R Using the caret Package. *Journal of Statistical Software*
467 28:1–26.
- 468 Larson, A. J., and D. Churchill. 2012. Tree spatial patterns in fire-frequent forests of western North America,
469 including mechanisms of pattern formation and implications for designing fuel reduction and restoration
470 treatments. *Forest Ecology and Management* 267:74–92.
- 471 Li, W., Q. Guo, M. K. Jakubowski, and M. Kelly. 2012. A New Method for Segmenting Individual Trees
472 from the Lidar Point Cloud. *Photogrammetric Engineering & Remote Sensing* 78:75–84.
- 473 Meyer, F., and S. Beucher. 1990. Morphological segmentation. *Journal of Visual Communication and Image
474 Representation* 1:21–46.
- 475 Micasense. 2015. MicaSense. <https://support.micasense.com/hc/en-us/articles/215261448-RedEdge-User-Manual-PDF-Download>
- 476 Millar, C. I., and N. L. Stephenson. 2015. Temperate forest health in an era of emerging megadisturbance.
477 *Science* 349:823–826.
- 478 Morris, J. L., S. Cottrell, C. J. Fettig, W. D. Hansen, R. L. Sherriff, V. A. Carter, J. L. Clear, J. Clement, R.
479 J. DeRose, J. A. Hicke, P. E. Higuera, K. M. Mattor, A. W. R. Seddon, H. T. Seppä, J. D. Stednick, and S.
480 J. Seybold. 2017. Managing bark beetle impacts on ecosystems and society: Priority questions to motivate
481 future research. *Journal of Applied Ecology* 54:750–760.
- 482 Negrón, J. F., J. D. McMillin, J. A. Anhold, and D. Coulson. 2009. Bark beetle-caused mortality in a

- 483 drought-affected ponderosa pine landscape in Arizona, USA. Forest Ecology and Management 257:1353–1362.
- 484 North, M. P., S. L. Stephens, B. M. Collins, J. K. Agee, G. Aplet, J. F. Franklin, and P. Z. Fule. 2015.
- 485 Reform forest fire management. Science 349:1280–1281.
- 486 Pau, G., F. Fuchs, O. Sklyar, M. Boutros, and W. Huber. 2010. EBImagean R package for image processing
- 487 with applications to cellular phenotypes. Bioinformatics 26:979–981.
- 488 Pebesma, E., R. Bivand, E. Racine, M. Sumner, I. Cook, T. Keitt, R. Lovelace, H. Wickham, J. Ooms, K.
- 489 Müller, and T. L. Pedersen. 2019. Sf: Simple Features for R.
- 490 Plowright, A. 2018. ForestTools: Analyzing Remotely Sensed Forest Data.
- 491 Popescu, S. C., and R. H. Wynne. 2004. Seeing the Trees in the Forest: Using Lidar and Multispectral Data
- 492 Fusion with Local Filtering and Variable Window Size for Estimating Tree Height. PHOTOGGRAMMETRIC
- 493 ENGINEERING:16.
- 494 Preisler, H. K., N. E. Grulke, Z. Heath, and S. L. Smith. 2017. Analysis and out-year forecast of beetle,
- 495 borer, and drought-induced tree mortality in California. Forest Ecology and Management. 399: 166–178
- 496 399:166–178.
- 497 R Core Team. 2018. R: A Language and Environment for Statistical Computing. R Foundation for Statistical
- 498 Computing, Vienna, Austria.
- 499 Raffa, K. F., B. H. Aukema, B. J. Bentz, A. L. Carroll, J. A. Hicke, M. G. Turner, and W. H. Romme. 2008.
- 500 Cross-scale Drivers of Natural Disturbances Prone to Anthropogenic Amplification: The Dynamics of Bark
- 501 Beetle Eruptions. BioScience 58:501–517.
- 502 Raffa, K. F., J.-C. Grégoire, and B. Staffan Lindgren. 2015. Natural History and Ecology of Bark Beetles.
- 503 Pages 1–40 in Bark Beetles. Elsevier.
- 504 Rouse, W., R. H. Haas, W. Deering, and J. A. Schell. 1973. MONITORING THE VERNAL ADVANCEMENT
- 505 AND RETROGRADATION (GREEN WAVE EFFECT) OF NATURAL VEGETATION. Type II Report,
- 506 Goddard Space Flight Center, Greenbelt, MD, USA.
- 507 Roussel, J.-R. 2019. lidRplugins: Extra functions and algorithms for lidR package.
- 508 Roussel, J.-R., D. A. (the documentation), F. D. B. (bugs and improved catalog features), and A. S. M. (lassnags).
- 509 2019. lidR: Airborne LiDAR Data Manipulation and Visualization for Forestry Applications.
- 510 Seidl, R., J. Müller, T. Hothorn, C. Bässler, M. Heurich, and M. Kautz. 2015. Small beetle, large-scale
- 511 drivers: How regional and landscape factors affect outbreaks of the European spruce bark beetle. The Journal

- 512 of applied ecology 53:530–540.
- 513 Shiklomanov, A. N., B. A. Bradley, K. M. Dahlin, A. M. Fox, C. M. Gough, F. M. Hoffman, E. M. Middleton,
514 S. P. Serbin, L. Smallman, and W. K. Smith. 2019. Enhancing global change experiments through integration
515 of remote-sensing techniques. *Frontiers in Ecology and the Environment* 0.
- 516 Shin, P., T. Sankey, M. Moore, and A. Thode. 2018. Evaluating Unmanned Aerial Vehicle Images for
517 Estimating Forest Canopy Fuels in a Ponderosa Pine Stand. *Remote Sensing* 10:1266.
- 518 Stephenson, N. 1998. Actual evapotranspiration and deficit: Biologically meaningful correlates of vegetation
519 distribution across spatial scales. *Journal of Biogeography* 25:855–870.
- 520 Stephenson, N. L., A. J. Das, N. J. Ampersee, and B. M. Bulaon. 2019. Which trees die during drought?
521 The key role of insect host-tree selection. *Journal of Ecology*:75.
- 522 USDAFS. 2019, February 11. Press Release: Survey finds 18 million trees died in California in 2018.
523 https://www.fs.usda.gov/Internet/FSE_DOCUMENTS/FSEPRD609321.pdf.
- 524 Vega, C., A. Hamrouni, S. El Mokhtari, J. Morel, J. Bock, J. P. Renaud, M. Bouvier, and S. Durrieu. 2014.
525 PTrees: A point-based approach to forest tree extraction from lidar data. *International Journal of Applied
526 Earth Observation and Geoinformation* 33:98–108.
- 527 Young, D. J. N., J. T. Stevens, J. M. Earles, J. Moore, A. Ellis, A. L. Jirka, and A. M. Latimer. 2017.
528 Long-term climate and competition explain forest mortality patterns under extreme drought. *Ecology Letters*
529 20:78–86.
- 530 Zhang, W., J. Qi, P. Wan, H. Wang, D. Xie, X. Wang, and G. Yan. 2016. An Easy-to-Use Airborne LiDAR
531 Data Filtering Method Based on Cloth Simulation. *Remote Sensing* 8:501.